Original Paper

New insights into the mechanism of surfactant enhanced oil recovery: Micellar solubilization and in-situ emulsification

Xue-Zhi Zhao [a], Guang-Zhi Liao [b], Ling-Yan Gong [a], Huo-Xin Luan [c], Quan-Sheng Chen [c], Wei-Dong Liu [d], Dong Liu [e], Yu-Jun Feng [a, *]

[a] Polymer Research Institute, State Key Laboratory of Polymer Materials Engineering, Sichuan University, Chengdu, 610065, People's Republic of China
[b] PetroChina Exploration & Production Company, Beijing, 100007, People's Republic of China
[c] Research Institute of Experiment and Detection, Xinjiang Oilfield Branch Company, PetroChina, Karamay, 834000, People's Republic of China
[d] Research Institute of Petroleum Exploration & Development, PetroChina Company Limited, Beijing, 100083, People's Republic of China
[e] Institute of Nuclear Physics and Chemistry, China Academy of Engineering Physics, Mianyang, 621000, People's Republic of China

A B S T R A C T

Reducing the oil-water interfacial tension (IFT) to ultra-low is believed the primary mechanism for surfactant-based enhanced oil recovery (EOR) process. However, field trials have shown that low concentration surfactant flooding can also improve oil recovery without ultra-low IFT. To clarify the mechanism behind, the currently-used surfactant, naphthenic arylsulfonate (NAS), was used to unravel its function during surfactant flooding from the horizon of micron- and nano-scale. The solubilization capacity of NAS micelle to petroleum fractions was evaluated through light absorbance strategy, small-angle neutron scattering, dynamic light scattering and transmission electron microscopy. It was found that micellar solubilization plays a significant role during the surfactant flooding. In-situ emulsification was visualized in microfluidics with three types of microchips, respectively. A series of displacement tests were carried out with NAS solution pumping into oil-saturated chip. The results show that in-situ emulsification improve oil recovery mainly through blocking and entrainment effects. Results from this work aid in understanding the interaction between surfactant solution and petroleum fractions at low surfactant concentration, which is helpful for design surfactant-based displacing system for EOR process.
© 2021 The Authors. Publishing services by Elsevier B.V. on behalf of KeAi Communications Co. Ltd. This is an open access article under the CC BY-NC-ND license (http://creativecommons.org/licenses/by-nc-nd/4.0/).

1. Introduction

After primary and secondary oil recovery process, there are still about two-thirds of the original oil trapped in geological reservoirs (Thomas, 2008). Due to its high efficiency and economic superiority, chemical enhanced oil recovery (EOR) methods particularly surfactant-based strategies have been devised and utilized in many matured oilfields (Gbadamosi et al., 2019). Previous researches generally believe that reducing the oil-water interfacial tension (IFT) to ultra-low level is the main mechanism of surfactant EOR process (Sheng, 2015). Generally, this process requires the strict formulation, which involves the relatively high concentration (>15 wt%) of surfactant or the presence of co-surfactant (Bera and Mandal, 2015). Nevertheless, a growing number of field

applications and lab researches indicate that low concentration (<0.3 wt%) surfactant flood can also boost oil recovery efficiently even without ultra-low IFT (Zhu et al., 2013; Wang et al., 2009). This inspired us to see through what happens between surfactant solution and crude oil at pore-scale or even nano-scale.

Generally, the ability of driving fluid to mobilize oil ganglia in porous reservoir rock mainly relies on the capillary number (N_c). The N_c is a dimensionless number which defined as (Chatzis and Morrow, 1984)

$$Nc = \frac{\mu v}{\sigma} \tag{1}$$

where μ is the viscosity, v the Darcy velocity of the driving fluid, and σ the oil-water IFT. Previously reported work have pointed out that when the N_c reaches 10^{-3}, the oil saturation can approach zero (Foster, 1973). Based on Equation (1), given that μ and v cannot increase thousand times practically, the only way to get such a high

N_c is to lower the IFT less than 10^{-3} mN·m^{-1} (Hu et al., 2017; Aoudia et al., 2006). It has been advocated for decades that such an ultra-low IFT value can be achieved by formulating middle-phase microemulsions with appriopriate package containing surfactant and cosurfactant or solvent (Jeirani et al., 2014). Therefore, surfactant flooding was also called microemulsion flooding in 1970s (Healy and Reed, 1977). However, it is picky to formulate microemulsion since several factors including surfactant type, electrolyte, cosurfactant type and their concentrations, influence the surfactant efficiency (Klier et al., 2000). Normally, a relatively high surfactant concentration and the presence of alkali is favorable for the preparation of microemulsion (Bera et al., 2015). Although it has been demonstrated that middle phase microemulsions can be obtained by using less than 1% of the surfactant, alkali such as Na$_2$CO$_3$ is indispensable in the system (Chen et al., 2018b). However, alkali has been used with increasing caution due to its possible side effects, such as scale formation and accelerating corrosion of pipes (Guo et al., 2017). For this reason, the alkali-free displacing formulations have attracted increasing attention from petroleum industry. Zhu et al. (2013) reviewed the recent progress of surfactant-polymer (SP) flooding application in China oilfields, and reported that an increase of approximately 1.8 million tons of oil production can be achieved annually by using SP flooding with low surfactant concentration (less than 0.4 wt%) and alkali-free formulation. Sun et al. (2020) reported that the maximum dosage of surfactant in the field tests in Liaohe, Dagang, and Xinjiang Oilfields is only 0.3 wt%, resulting a IFT just at the magnitude of 10^{-2} mN·m^{-1}, which is obviously higher than the ultra-low value for microemulsion formation (Jeirani et al., 2013). Nevertheless, about 0.35 million tons of oil were produced in above three oilfields in 2019 with an average oil recovery factor around 18% (Sun et al., 2020). Such a significant recovery factor cannot be ascribed solely by IFT reduction mechanism. Therefore, it is necessary to regain insight into the mechanism of surfactant EOR.

In recent decades, in-situ emulsification was believed a potential possibility to produce more oil (Liu et al., 2020; Hirasaki et al., 2011). Previous researches (Liu et al., 2019) have shown that emulsions can be formed during surfactant EOR process. For instance, Chen and co-workers (Chen et al., 1991) observed that part of driving fluid would flow in the form of emulsion during a core flooding, indicating that emulsion could be created on-site, which is very different from the separate two-phase flow of oil and water during water flooding. Nevertheless, due to the complexity of the porous reservoir rock, the physics of emulsification process is rarely evaluated (Kokal et al., 1992). Therefore, exploring the potential mechanisms involved in the flow of multiple phases in porous media is a key to reveal the exact course of in-situ emulsification and its contribution to EOR. However, previous studies have generally been carried out in natural or artificial cores (Kokal et al., 1992; McAuliffe, 1973; Guillen et al., 2012a), in which emulsification can only be studied indirectly by analyzing the pressure fluctuation and the eluates, the realistic emulsification process is still ambiguous due to its invisibility. To address this issue, our previous work (Zhao et al., 2020) employed microfluidic devices to monitor the in-situ emulsification process between sodium 4-dodecylbenzenesulfonate (SDBS) solution and paraffin oil in two-dimensional (2D) microfluidics. Nevertheless, the oil and surfactant employed there were simplified to model substitutes, which were very different in chemical composition from the crude oil and the surfactant used in field trials. Besides, despite the flow behavior of multiple phase can be directly observed in a 2D microchip, it is impossible to obtain the parameters associated with the porous connection in 3D scale. A three-dimensional (3D) model can thus better simulate the complex geometric characteristics of the realistic porous media.

Unlike emulsion systems that have been widely concerned by petroleum industry, very little research has been done to explore whether surfactant micelles play a role during EOR process. Undoubtedly, amphiphilic molecules can self-assemble to form colloidal-size clusters in solution once its concentration exceeds the critical micellar concentration (Rosen and Kunjappu, 2012; Gong et al., 2019). It was reported previously that the hydrophobic interior of micelles can solubilize drugs (Torchilin, 2007), dyes (Tehrani-Bagha and Holmberg, 2013) and oil (Lindén et al., 2000). Although plenty of work was dedicated to the solubilization effect of micellar systems on hydrophobic substances, few reports focused on micellar solubilization in surfactant EOR process. Recently, Gong et al. (2020) used SDBS as model surfactant and anisole (or 1-hexene) as solubilizate to check the solubilization capacity and the evolution of micelles upon solubilization. They observed that the SDBS micelles can indeed load oil phase, and thus proposed micellar solubilization as a supplementary explanation for surfactant enhanced oil recovery without ultra-low IFT. Nevertheless, as mentioned above, the solubilization tests based on model substitutes can not fully represent the realistic EOR process.

To investigate the surfactant EOR mechanism more realistically, herein, naphthenic arylsulfonates (NAS), a currently-used surfactant in Karamay oilfield of PetroChina, was selected to systematically examine its solubilization capacity and emulsification behavior. Generally, the industrial NAS is derived from the local oil cracking components, and its main ingredient has been confirmed as benzodicyclohexane sulfonate, with multiple minorities such as alkyl indan sulfonate and alkyl benzene sulfonate (Luan et al., 2019). As for oil phase, to keep the research closer to reality, the alkanes and aromatics, which were extracted from crude oil, were emloyed in this work to mimic the residual oil in reservoir porous media.

This work focused on two aspects, namely, micellar solubilization and in-situ emulsification, to shed light on the interaction between NAS solution and petroleum components. On one hand, a series of tools including UV−Vis spectroscopy, SANS and DLS were employed to determine the solubilization capacity of NAS micelles to pertroleum fraction, and to monitor the solubilization parameters including micellar size, solubilizates location and micellar morphology. On the other hand, microfluidics was employed to investigate the in-situ emulsfication process during the surfactant flooding. The O/W and W/O emulsification process was visualized in 2D and 3D micromodels, with which the contribution of emlsification to improve oil recovery was quantified by analysing eluates and pore-scale snapshots. It shoul be noted that all the experiments were conducted at 40 °C to mimic the reservoir environment of Karamay Oilfield.

2. Experimental section

2.1. Materials

NAS was kindly offered from Lanzhou Institute of Chemical Physics (LICP), Chinese Academy of Sciences (Lanzhou, China) (Luan et al., 2019) and the main ingredient was displayed in Scheme S1. The oil phases, alkanes and aromatics separated from crude oil having viscosity of 24 and 44 mPa·s at 40 °C, respectively, were also donated by LICP. Nile Red (99%, GC; Sigma-Aldrich, USA), Fluorescein (99%, GC; J&K, China) and Isopropyl alcohol (99.7%, AR, Chron Chemicals, China) were used without any further treatment. An ultrapure water system (UPH−I-10T, Chengdu Science and Technology Co., Ltd., China) was used to produce ultrapure water with resistivity of 18.25 MΩ·cm.

2.2. Interfacial tension

The interfacial tension between aqueous solution of NAS and alkanes (or aromatics) was determined by utilizing a spinning drop tensiometer (CNG TX500C, USA). A drop of oil was suspended in a capillary filled with aqueous phase and placed in the measuring chamber. The rotate speed was maintained at 5000 rpm, and the snapshots of oil droplets were captured accordingly. The results were obtained by calculating the length and width of the oil droplets. Each test was performed at 40 °C for 1 h until the measured data was constant.

2.3. Dynamic light scattering (DLS)

The size of micelles was determined on a Zetasizer Nano system (ZS90, Malvern Instruments, UK) at 40 °C. The setup contains a He−Ne laser source operating at a wavelength of 633 nm, and the scattered light was emitted at an angle of 173°. The diffusion co-efficients were determined by analyzing the light intensity fluctu-ations, and then the particle size was obtained by using the software Mastersizer 2000 based on Stokes-Einstein equation.

2.4. UV−vis spectroscopy

The solubilization capacity of NAS micelles was quantified by light absorbance. A UV−Vis spectrophotometer (UV-6100, Mapada, China) with dual channel was employed to detect the fluctuation of the light absorbance at 600 nm during the addition of oil to NAS solution. One of the channels was used for pure NAS solution as a reference, and the other one for NAS/oil solution, offsetting the error caused by the light source. All the tests were operated at 40 °C.

2.5. Small-angle neutron scattering (SANS)

SANS tests were carried out at Mianyang Research Reactor owned by China Academy of Engineering Physics. The specific subsystem and experimental parameters were basically consistent with our previous work (Zhao et al., 2021) and described in sup-porting information.

2.6. Transmission electronic microscope (TEM)

TEM visualization was performed on a Hitachi H600 trans-mission electron microscope with an acceleration voltage of 75 kV. The specimens for TEM observation were prepared as follows: about 20 μL of sample solution was added to a copper grid, followed by staining with 1.0 wt% phosphotungstic acid solution for a few minutes, and then dried under a roast lamp prior to visualization.

2.7. 2D and 3D microfluidics

The specific subsystem and schematic illustration of micro-fluidic setup were depicted in supporting information (Fig. S1). Three microchips were employed in this work. Both of the 2D chips were prepared in our previous work (Zhao et al., 2020), the 3D model was prepared according to a previous work (Datta et al., 2013) by sintering packed hydrophilic glass beads. The appear-ance and parameters of all chips (Fig. S2), as well was the procedure of microfluidic experiments were displayed in supporting information.

3. Results and discussion

3.1. IFT between oil phase and NAS solution

As aforementioned, reducing the oil-water IFT to ultralow level is believed to be the primary mechanism of surfactant EOR. Therefore, it is necessary to determine the IFT of the systems in this work prior to the subsequent tests. Exhibited in Fig. 1 is the vari-ation of IFT between petroleum fractions and aqueous solution of NAS with time at 40 °C.

As can be seen in Fig. 1a, for NAS/alkanes system, the IFT starts at 2.21 and 1.40 mN·m^{-1} when the NAS concentration is 0.1 wt% or 0.2 wt%, respectively, and remain almost unchanged over 60 min. As the NAS concentration increases to 0.4 wt%, the initial value of IFT decreases to 0.33 mN·m^{-1} and eventually stabilizes at 0.53 mN·m^{-1} after 60 min of ascent. It is obvious that none of above pairs can achieve ultralow IFT, since a typical ultralow value need to on the order of 10^{-3} mN·m^{-1}. The decreasing tendency of IFT value with the increase of surfactant concentration can be explained as follows: with the addition of NAS, more and more amphiphilic molecules aggregate at the oil-water interface to form interfacial membrane, which enhances the surface pressure, lead-ing to the descrease of interfacial energy and IFT (Zhao et al., 2013). Similar to NAS/alkanes system, as shown in Fig. 1b, the IFT between NAS solution and aromatics shows the same trend. At the NAS concentration of 0.1 wt%, 0.2 wt% and 0.4 wt%, the IFT are 2.53, 1.37 and 0.36 mN·m^{-1}, respectively.

Since above systems do not achieve ultralow IFT, classical mechanisms cannot be used to explain the role of surfactant flooding (Sheng, 2015). Therefore, it is urgent to propose an alter-native mechanism to clarify how surfactant flooding improve oil recovery.

3.2. Micellar solubilization

As mentioned in the "Introduction" part, micelles show solubi-lizing ability once the surfactant concentration goes above CMC. In this section, a series of measurements were conducted to deter-mine the contribution of micelle solubilization to surfactant EOR.

3.2.1. Solubilization capacity of NAS micelle to petroleum fractions

First, the solubilization capacity of NAS micelles to petroleum fractions were determined by light absorbance measurements ac-cording to previous report (Nguyen-Kim et al., 2016). Fig. 2a and b compare the change of absorbance of NAS solution with gradient concentration against the addition of alkanes or aromatics. Taking 0.2 wt% NAS solution as an example, as shown by the red dots in Fig. 2a, when alkanes concentration is lower than 0.78 mg·ml^{-1}, the absorbance maintains constant, then climbs abruptly once the alkanes concentration exceeds this threshold. The inset in Fig. 2a depicts the evolution of 0.2 wt% NAS solution from transparent to turbid during the loading of alkanes from 0.1 to 2.5 mg·ml^{-1}, further revealing the solubilization effect of NAS micelles on alkanes.

We performed piecewise linear fitting for the light absorbance data, and the maximum solubilized amount of additives in NAS micelles can be acquired from the intersection of the fitted lines. Below this inflection point, the micelles loaded with additives are also namely "swollen micelles" (Tehrani-Bagha et al., 2012). Nevertheless, once the interior of micelles was filled with additives, the excess alkanes could only be dispersed in the solution as a separate phase, herein, under the mechanical agitation, an epi-nephelos O/W emulsion system was formed. The same strategy was conducted in the NAS/aromatics system, and a similar trend can be found. As exhibited in Fig. 2b, the turning points represent that up
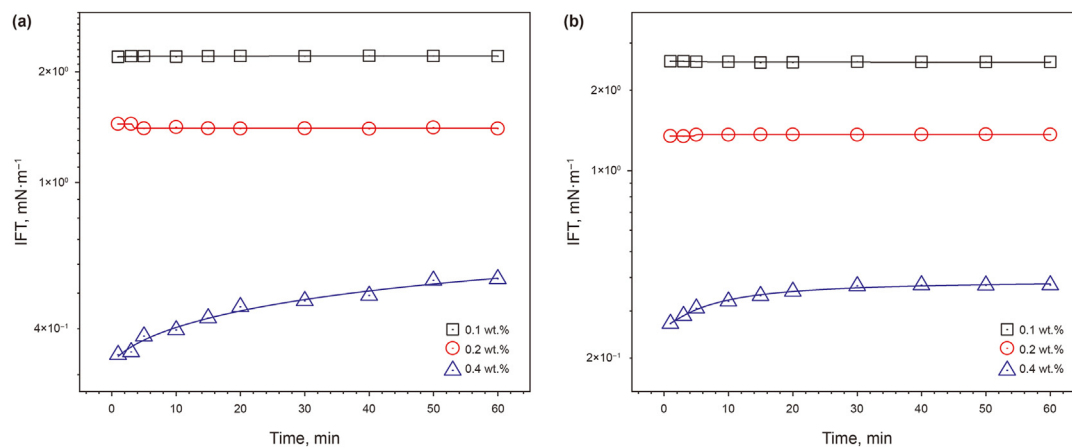
Fig. 1. Dynamic IFT between **(a)** alkanes or **(b)** aromatics and different concentration of NAS at 40 °C.
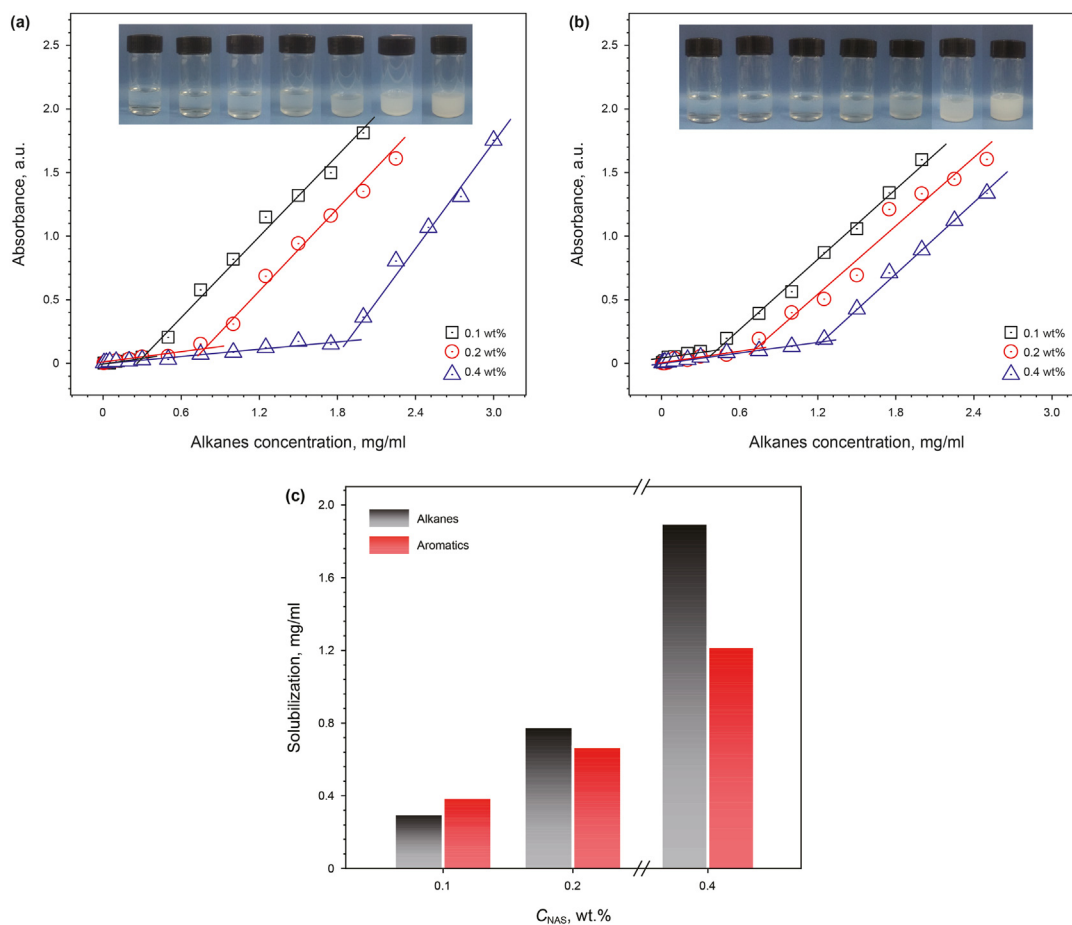

Fig. 2. Light absorbance of NAS solution with different concentration during the loading of **(a)** alkanes and **(b)** aromatics; **(c)** The solubilization capacity of 0.1 wt%, 0.2 wt% and 0.4 wt% NAS solution to alkanes and aromatics. The insets depicted the opacification of 0.2 wt% NAS solutions during the loading of oil phase. All the tests were performed at 40 °C.

to 0.39, 0.67 and 1.22 mg·ml^{-1} aromatics can be loaded in 0.1 wt%, 0.2 wt% and 0.4 wt% NAS solution, respectively.

Fig. 2c reflects the effect of surfactant concentration on micellar solubilization, and all the results are summarized from the cross piont in Fig. 2a and b. It is not difficult to imagine that the higher the surfactant concentration, the more micelles can be formed. In addition, as reported previously (Gong et al., 2020), increasing the surfactant concentration will enhance the micellization effect and

enlarge the inner space of micelles, thus allowing more alkanes to be absorbed.

Moreover, one can find from Fig. 2 that the maximum solubilized amount of alkanes in NAS solution seems higher than that of aromatics, especially at high NAS concentration. In 0.4 wt% NAS solution, the solubility of alkanes is 1.5 times that of aromatics, which can be explained by the structural difference of the additives (Tehrani-Bagha et al., 2012). Since the π-conjugated benzene rings

give aromatics a planar molecular configuration, it is awkward for such a rigid molecule to be solubilized into the micellar core, and can only be confined to the palisade layer with limited space. For alkanes, its structure is more flexible and similar to the hydrophobic chain of surfactant molecule, thus can be incorporated into the micellar core. The solubilization location mentioned above will be verified in Section 3.2.2.

According to above quantified data, it can be concluded that micellar solubilization effect cannot be ignored during the surfactant EOR process, especially at low surfactant concentration without ultralow IFT. The maximum solubilized amount of alkanes and aromatics in 0.2 wt% NAS solution is 0.78 and 0.67 mg·ml^{-1}, respectively. Based on this ratio, it can be inferred that 780 g alkanes and 670 g aromatics can be solubilized in 1 ton of 0.2 wt% NAS solution in the practical trial. This is probably why surfactant solutions without ultralow IFT can also enhance oil recovery.

3.2.2. Solubilization site of petroleum fractions in NAS micelles

Since petroleum fractions were indeed solubilized in NAS micelles, it is logic to further check the exact location of additives in micelles. It is reported that the solubilization site can be determined through several tools such as UV−Vis spectroscopy (Vermathen et al., 2000), NMR spectroscopy (Wu et al., 2005), and X-ray diffraction (Chiang, 2001). Herein, UV−Vis spectroscopy strategy was used to examine the exact site of petroleum fractions in NAS micelles.

The UV−Vis absorption of the additives in NAS solutions were compared with its spectra in polar (methanol) and non-polar (n-heptane) solvents. As shown in Fig. S4a, alkanes in NAS solution has a similar spectrum to that in n-heptane, thus we can infer that the alkanes are solubilized in the non-polar micellar core. For aromatics, the maximum absorption peak of aromatics-containing NAS solution is closer to its absorption in methanol (Fig. S4b), indicating that the aromatics are most likely situated in the palisade region with moderate polarity. It should be pointed out that, as a reference curve, the UV−Vis absorption of alkanes and aromatics in methanol and n-heptane have been measured in our previous work (Zhao et al., 2021), so we used them directly here.

3.2.3. Micellar size change during solubilization

To shed light on the micellar swelling process, DLS measurement of 0.4 wt% NAS micellar systems was conducted with the addition of additives. Fig. 3a depicts the micellar size change during the solubilization of alkanes in NAS solution. Before loading with alkanes, a monodispersed peak appeared with a particle size of

126 nm in diameter. Once 0.25 mg·ml^{-1} alkanes was loaded, the diameter gradually increased to 139 nm. When the concentration was further increased to 1.5 mg·ml^{-1}, the micelles significantly grew to 240 nm. According to the results in section 3.2.1, up to 1.9 mg·ml^{-1} alkanes can be solubilized in 0.4 wt% NAS solution, when the concentration of alkanes is below this value, the solution remains transparent, with a gental increase in particle size. However, once the alkane concentration exceeds this threshold, as shown by the topmost curve in Fig. 3a, a peak at 2072 nm is observed, indicating the formation of oil droplets. It should be noted that multimodal distribution was observed when 2.5 mg·ml^{-1} alkanes was added, among which the peak at 2072 nm comes from the oil-in-water emulsion, while the peak at 172 nm is attributed to the micelles.

Analogously, for the NAS/aromatics system, the micellar size shows the same trend. As displayed in Fig. 3b, when the aromatics concentration increased from 0 to 1.0 mg·ml^{-1}, the micellar size increased slightly from 126 nm to 232 nm. However, once the aromatics amount exceed its maximum solubility in NAS solution (1.2 mg·ml^{-1} in 0.4 wt% NAS solution), as depicted by the topmost curve in Fig. 3b, when 1.5 mg·ml^{-1} aromatics was loaded, a peak at 1176 nm can be observed, indicative of the formation of emulsions.

TEM and SANS were then used to track the change in the micellar size before and after loading additives. Plotted in Fig. 4a is the TEM image of NAS micelles without solubilizates, and spherical micelles with a diameter of ~32 nm can be observed. It is worth noting that the particle size determined from TEM image is much smaller than that measured by DLS. Such conflict is in agreement with previous report (Zhao et al., 2018) which proposed that the TEM reflect the microstructure in dehydrated state, while DLS tests obtain the hydrodynamic size in solution. After loading with 1.5 mg·ml^{-1} alkanes, as depicted in Fig. 4b, the micelles remain spherical morphology but increased in size from around 32 to ~40 nm, which verified the swelling process. Similarly, for the NAS/aromatics system, as shown in Fig. 4c, the presence of 1.0 mg·ml^{-1} aromatics did not change the micellar shape, but increased the size to ~42 nm, which also proved the loading of aromatics in micelles.

More convincing evidence of microstructural changes were reflected in the SANS data. Fig. S5 shows the scattering intensity (I) as a function wave-vector (q) for 0.4 wt% NAS solution with and without solubilizates. One can find from Fig. S5a that the curves show different trend with the loading of alkanes. When 1.5 mg·ml^{-1} alkanes was solubilized, the curve remain the same shape with that of unloaded system, but a slight climb in I at low q area, indicating the entrance of additives in aggregates. We used a
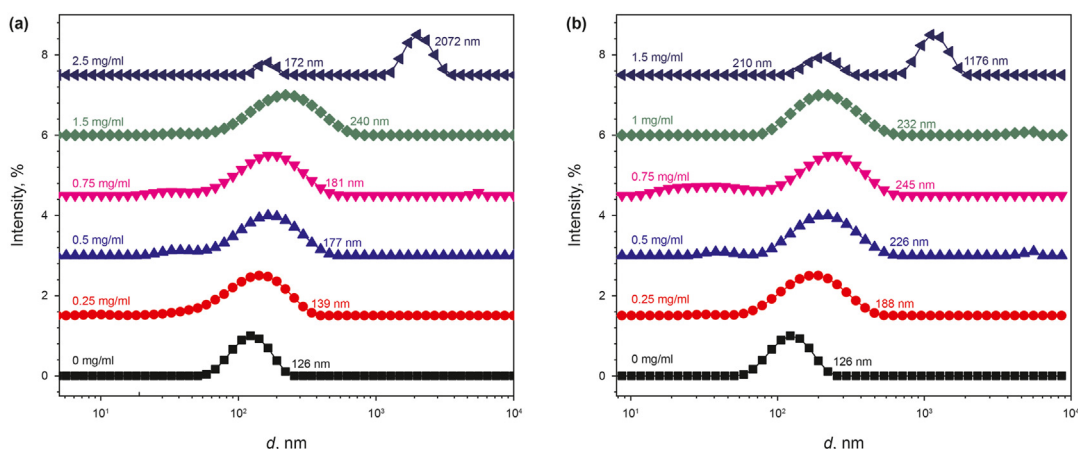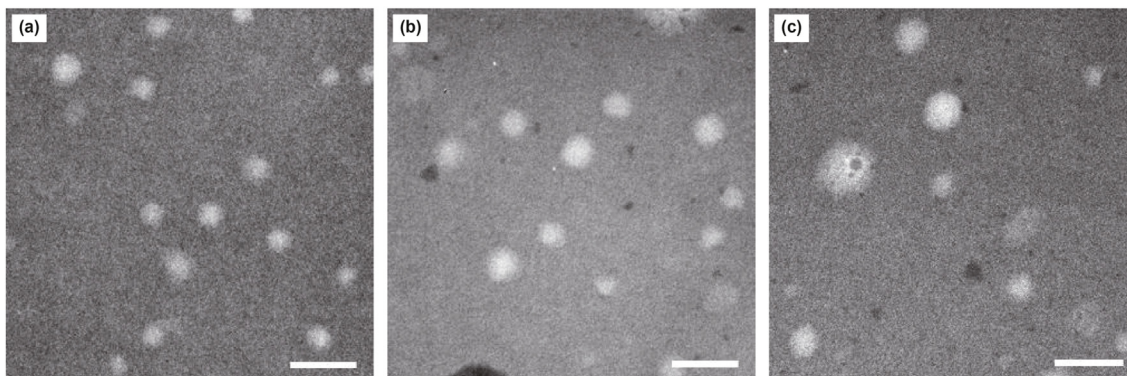

Fig. 3. Variation of micellar size in 0.4 wt% NAS solutions at different concentration of (a) alkanes and (b) aromatics.

Fig. 4. TEM images of **(a)** 0.4 wt% NAS micellar solution and 0.4 wt% NAS micellar solution loaded with **(b)** 1.5 mg·ml^{-1} alkanes and **(c)** 1.0 mg·ml^{-1} aromatics. The scale bar is 50 nm.

polydisperse sphere model conjugated with a Hayter–Penfold potential (Hayter and Penfold, 1981) to fit the SANS curve, and the results proved the formation of spherical micelles. However, once the alkanes concentration exceed its maximum solubility in NAS solution, as shown by the blue curve in Fig. S5a, the scattering intensity climbs dramatically at low q domian, which probably originated from the formation of micron-scale particles in solution. Similar tests were carried out with aromatics as solubilizates. As can be seen in Fig. S5b, when 1.0 mg·ml^{-1} aromatics was solubilized, the scattering intensity slightly increase at low q region, indicating the aromatics were swollen the micelles. Further increased the aromatics concentration to 1.5 mg·ml^{-1}, the scattering intensity increases significantly at low q region (see the blue curve in Fig. S5b), indicative of micron-scale oil droplets formed in solution.

To sum up, the DLS, TEM and SANS tests revealed the micellar swelling process during the loading of petroleum fractions; and the transformation from swollen micelle to O/W emulsion once the additives amount exceeds the solubilization capacity. From the above experiments, we can conclude that micelles can indeed solubilize crude oil components and this effect is obviously conducive to enhanced oil recovery.

3.3. In-situ emulsification in microfluidics

3.3.1. O/W emulsification in 2D microchip

Since above section shown that emulsion can be formed once the oil concentration exceed the solubilization capacity of micellar solution, it is interesting to find out whether the emulsification could occur in-situ during the surfactant flooding. Actually, during the past decades, in-situ emulsification has been considered as an alternative mechanism for ascribing surfactant EOR (Kokal et al., 1992; McAuliffe, 1973; Guillen et al., 2012a). Herein, microfluidic experiments were carried out to directly visualize the emulsification process during NAS flooding, and to quantify its contribution to surfactant EOR.

First, the microfluidic experiments were conducted in a 2D micromodel with random pore structure to mimic the displacing process in porous media. The properties of displacing and displaced phase, as well as the volume of eluate are summarized in Table 1. It should be noted that the injected volume for each group is 1500 μl.

Prior to surfactant displacement, pure water was pumped into the alkanes or aromatics saturated micromodel respectively as the control. Fig. S6 provides a view of displacement results after 2 h of water injection, one can find that the residual oil in micromodel exists in the form of large ganglia, which generally occupies several pore spaces. Moreover, emulsion droplet with typical spherical

Table 1
The displacement results in 2D heterogenous chip with different displaced phases and displaced fluids.

Run	$C_{NAS,}$ wt.%	Oil	Emulsion volume, μL	Oil volume, μL	Total volume, μL
1	0	alkanes	0	196.0	196.0
2	0.2	alkanes	23.0	247.5	270.5
3	0	aromatics	0	182.2	182.2
4	0.2	aromatics	17.6	224.1	241.7

shape was not found in the porous media due to absence of surfactant. Fig. 5 provides the view of eluate collected from all groups. As displayed in Fig. 5a and c, only pure alkanes and aromatics exist in the upper layer of the eluate, and no emulsion was found in the tube, which further proved that no emulsification occurred due to the absence of surfactant. After 1500 μl of water was injected respectively, 196.0 μl of alkanes or 182.2 μl aromatics were collected from the eluate.

Further experiments were conducted with 0.2 wt% NAS solution as the driving fluid and the experimental parameters were consistent with that of blank control. As depicted in Fig. 5b and d, opalescent liquids appeared in the glass tubes, above and below which are alkanes (or aromatics) and NAS solution, respectively. The opalescent phase from Run 2 (Fig. 5b) was sucked out with a syringe and observed under fluorescent microscope (Fig. 5e), which verified that it is indeed an O/W emulsion. Fig. 6 provides a view in micromodel during the injection of 0.2 wt% NAS solution, one can find that obvious emulsification occurred in both alkanes and aromatics systems, and spherical droplets with regular shape could be observed under normal and excitation light. To evaluate more precisely the emulsifying effect, Fig. 6b and e were analyzed by using Digimizer software to calculate the size and size distribution of all individual oil droplets, and the quantitative results are displayed in Fig. 6c and f, and summarized in Table S1. When 0.2 wt% NAS solution was injected into an alkanes saturated model, oil droplets with average diameter of 124 μm were formed, which were smaller than that of aromatics counterpart (147 μm in diameter). A smaller size of emulsion indicates a better emulsifying effect, which may be originated from the difference in oil viscosity (Chen et al., 2018a).

It has been demonstrated in above experiments that in-situ emulsification dose occurs in the porous model, it is interesting to reveal how emulsion is produced. Herein, a complete emulsification process has been recorded by a high-speed camera and displayed in Fig. 7 and Movie S1 (Run 2 in Table 1). When the residual oil was pushed to the pore throat by displacing fluid (0 ms),
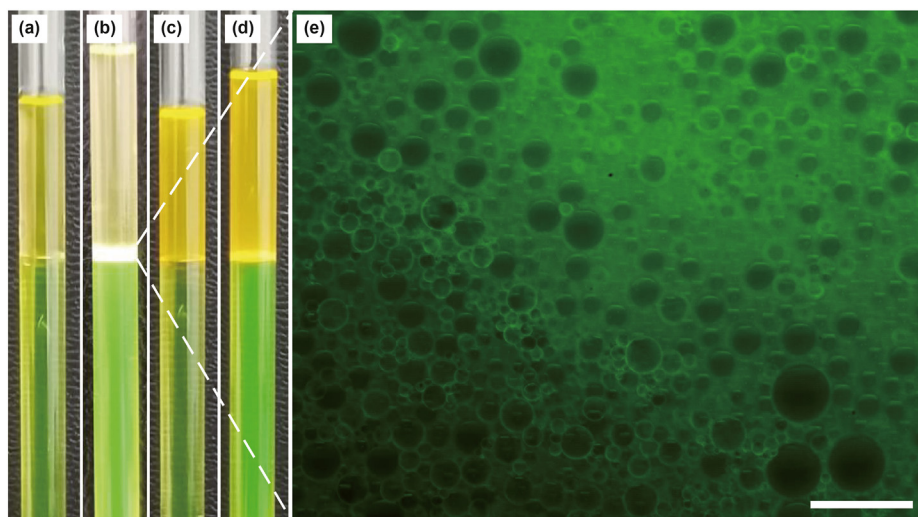
Fig. 5. Images of eluate collected from the injection of (**a** & **c**) water and (**b** & **d**) 0.2 wt% NAS solutions into (**a** & **b**) alkanes and (**c** & **d**) aromatics saturated microchip. The displacing fluid was injected at a flow rate of 10 μl·min⁻¹ and all the tests were carried out at 40 °C. Fluorescent image (**e**) of the emulsion collected from Run 2, Table 1 $\lambda_{ex} = 420-485$ nm. The scale bar is 500 μm.
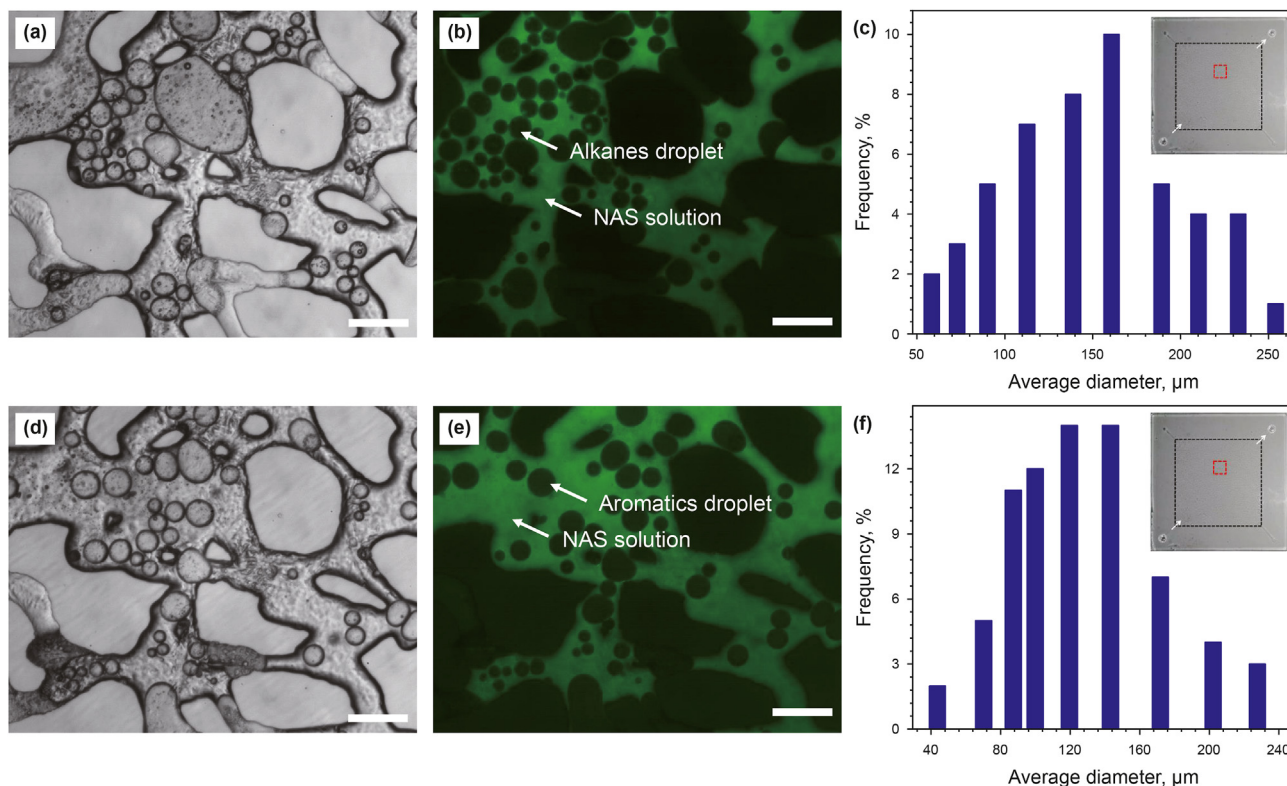


Fig. 6. Images taken from the flow of 0.2 wt% NAS solutions in alkanes (**a** & **b**) and aromatics (**d** & **e**) saturated micromodel. (**a** & **d**) were captured under normal light, while (**b** & **e**) under 420–485 nm excitation light. (**c** & **f**) shows the droplet size distribution in (**b** & **e**), respectively. Displacing fluids were injected at 10 μl·min⁻¹ at 40 °C. The scale bar is 500 μm.

as the capillary resistance is greater than the displacement pressure, the leading edge of the ganglia is rapidly extruded within 0–350 ms, and finally snapped off at 400 ms; however, the main part of the residual oil was still intercepted by capillary resistance. The extruded oil evolved into spherical shape (see the inset captured at 400 ms), forming pore-throat scale emulsion and flowing to downstream.

Supplementary video related to this article can be found at https://doi.org/10.1016/j.petsci.2021.11.014

In addition, the pressure drops (ΔP) between inlet and outlet of Run 1–4 were recorded and depicted in Fig. S7. When pure water was injected to displace alkanes, as shown by the red curve in Fig. S7A, the ΔP increased rapidly in the early stage, reaching a peak at ~9.9 kPa, and then decreased gradually until stabilized at ~2.0 kPa. The highest pressure reflected the maximum resistance achieved in the flow paths, which corresponded to the lowest total mobility (Gogarty et al., 1970). As the oil was displaced, the flow resistance declined, and then the ΔP decreased. As for NAS/alkanes
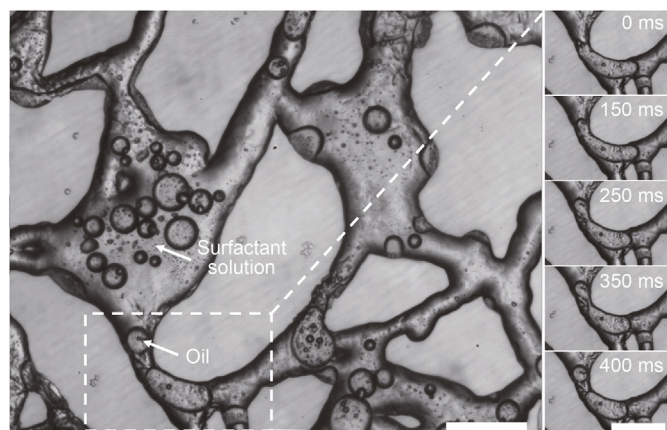
Fig. 7. Emulsification process during the injection of 0.2 wt% NAS solution into alkanes saturated model at 40 °C. The flux is 10 μl·min⁻¹ and the scale bar is 500 μm.

system (see the black curve in Fig. S7), the ΔP increased with the advancement of aqueous injection, and reached the peak at ~18.2 kPa. Then it decreased and stabilized at ~5.2 kPa, significantly greater than that of control case, indicative of the existence of pore-scale emulsion, which acts as a plugging agent and compensates the pressure drop (Guillen et al., 2012b). As a result, the compensation of pressure decline by in-situ emulsion is conducive to the spread of displacing fluid to a wider area, thus the sweep efficiency is improved.

Fig. 8 shows the macroscopic displacement result. As displayed in Fig. 8a, when water was pumped into the alkanes saturated model, the displacing fluid can only sweep 65% of the whole area (the region surrounded by blue curves), and such a low sweep efficiency is certainly not conducive to improve oil recovery. When 0.2 wt% NAS solution was used, as shown in Fig. 8b, the swept region is extended to almost the entire model, with a sweep efficiency increase of approximately 35%, which is undoubtedly beneficial for enhancing oil recovery.

Analogously, for NAS/aromatics system, as displayed in Fig. S7b, the ΔP show the same trend. It should be noted that the ΔP of aromatics group is significantly higher than that of alkanes group, which could be attributed to the higher viscosity of the aromatics. Similarly, in-situ emulsification also leads to an improvement in sweep efficiency. As shown in Fig. 8c and d, the use of surfactant increased sweep efficiency by about 25% compared to pure water injection.

In summary, the above tests show that in-situ emulsification can improve oil recovery mainly through blocking effects, which optimize the sweep efficiency, leading to an incremental alkanes of 26% and aromatics of 23% over waterflooding.

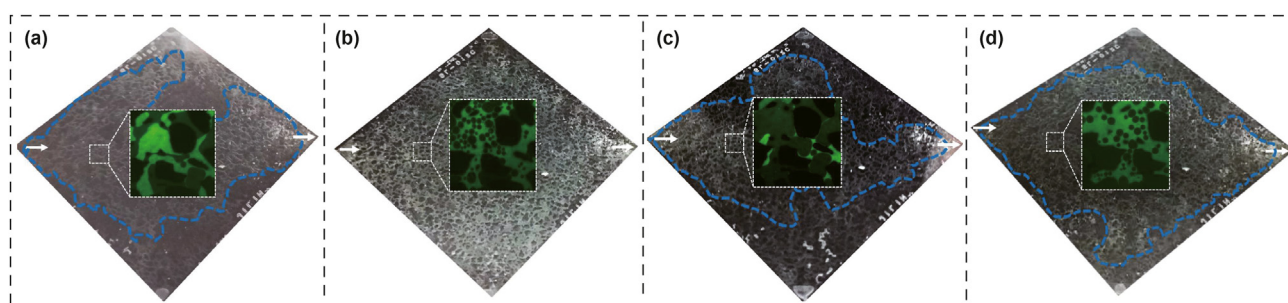### 3.3.2. W/O emulsification in 2D microchip

It has been reported that W/O emulsification also improve oil recovery, though to a lesser extent, through decreasing the effective viscosity of oil (de Haas et al., 2013). In this work, the W/O emulsion droplets were also observed in above injection tests; however, due to the irregularity of channel, it is difficult to predict the area where W/O emulsification occurs, which make it impossible to record a complete emulsification process. Recently, Unsal et al. (Broens et al., 2018) proposed a glass-etched microchip, in which the oil phase could be fixed in the dead-end extension. Herein, we used it as a dedicated platform to investigate the W/O emulsification process.

As a blank control, pure water was pumped into the oil saturated chip at a flux of 0.1 μl·min⁻¹. After 3 h of injection, no water droplet was found either in alkanes or aromatics system (Fig. S8), indicating that W/O emulsification never occurred due to the absence of surfactant.

Fig. 9 shows the penetration process of NAS solution into trapped alkanes. It is observed that the trapped oil remains unchanged at the initial stage of displacement (Fig. 9a). After 20 min of injection, small water drops began to penetrate into oil phase at the junction of branch extension and main channel (Fig. 9b). Then, the water drops at the T-junction grew to several microns in diameter (Fig. 9c), and the emulsified range expanded and reached the dead end at 90 min (Fig. 9d). Subsequently, the water drops gradually grew in size and stabilized at 300 min. As a supplementary, Fig. 9g−9l show emulsification process under fluorescent excitation, and the green dots in trapped oil further confirmed the existence of aqueous drops in oil phase. In short, W/O emulsification in dead-end channel is similar to a moth-eaten process. On the one hand, the aqueous phase invades the oil ganglia along the channel wall and flows into oil body like a wormhole, squeezing the space occupied by trapped oil, forcing it to move towards the main channel and being driven out by the displacing fluid. Secondly, due to the smaller viscosity of dispersed phase, the diffusion of small water droplets into oil phase will reduce the effective viscosity of residual oil (de Haas et al., 2013), which is beneficial to improve the mobility ratio, and thus, improve oil recovery. Similarly, the W/O emulsification process in NAS/aromatics system was also recorded according to the same experimental procedure (Fig. S9). The contribution of W/O emulsification was quantified by calculating the volume occupied by water drops through image analysis, ~12% trapped alkanes and ~10% aromatics can be displaced through W/O emulsification.

3.3.3. Displacement in 3D micromodel

The above experiments on 2D model proved that in-situ emulsification does occur during the NAS flooding. However, despite the advantage of visualization, the 2D model is quite different from the underground porous medium. For example, the pore structure of a 2D model is greatly less connected than that of a 3D medium; this

Fig. 8. Macroscopic displacement results from the injection of (a & c) water and (b & d) 0.2 wt% NAS solutions into (a & b) alkanes and (c & d) aromatics saturated microchip.
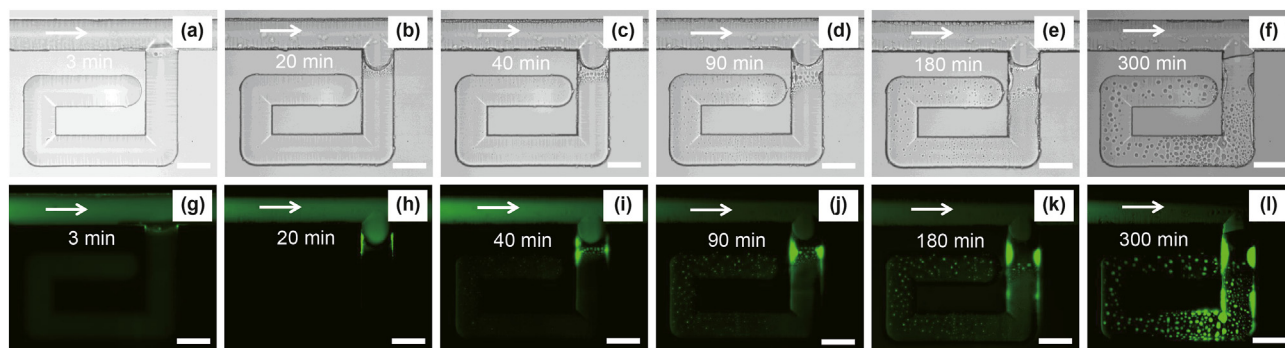
Fig. 9. W/O emulsification process in a dead-end channel initially filled with alkanes. 0.2 wt% NAS solution was pumped into model at a flux of 0.1 μl·min^{-1} at 40 °C. Images were captured under normal light (**a**–**f**) and 420–485 nm excitation light (**g**–**l**). The scale bar is 100 μm.

enhances the propensity of the non-wetting fluid to break up under 2D condition (Datta et al., 2014); in other words, emulsification is more likely occur in a 2D media, and thus, the applicability of such processes to 3D porous medium remains elusive. Herein, a glass beads sintered model was prepared to investigate the emulsification on 3D condition.

Fig. S10 shows the 3D rendering of the oil saturated porous media in a $640 \times 640 \times 250$ μm^3 volume area. As mentioned before, due to being labelled with Nile Red, the oil phase emits distinct fluorescence under excitation, which distinguishes it from the pore body. As shown in Fig. S10, the oil phase presents a three-dimensional network, while the black hole represents the space occupied by glass beads. One can find that almost all the pore and throat spaces were filled with oil phase after the oil saturation process.

Similar to previous tests, waterflooding was conducted in 3D model as a blank control. Fig. 10a and b depict the 3D rendering of the residual oil after 1500 μL water was injected. One can find that although the oil net is broken at some junctions, residual oil trapped in the medium still keeps the form of large ganglia, reflecting a poor displacement. The trapped volume of the oil phase was examined by image analysis, and the final oil saturation is calculated to 79% and 81%, respectively (Table 2). Such a high value came from the low value of capillary number (do Nascimento et al., 2019). Due to the high IFT between pure water and oil phases (34 mN·m^{-1} for water/alkanes system and 36 mN·m^{-1} for water/aromatics group), the N_c calculated was 1.4×10^{-6} and 1.3×10^{-6}, respectively (Table S2), and the viscous force is not high enough to overcome capillary force and mobilize more oil phase (Berg et al., 2013). The eluates in both cases were collected and quantified. As shown in Fig. S11 and Table 2, 233 μL of alkanes and 226 μL of aromatics were collected, and no emulsion was found in both cases.

Further tests were carried out with 0.2 wt% NAS solution as displacement agent. For NAS/alkanes system, after the injection of 1500 μL NAS solution, as shown in Fig. S11b, opalescent emulsion was observed in the eluate, indicating that the in-situ emulsification occurred in the porous media. The volume of emulsion obtained was 119 μL (Table 2), accounting for 50% of the pure alkanes. Such a significant emulsion amount indicates that the trapped oil can be emulsified and displaced, resulting in improved oil recovery efficiency.

The flow of oil droplets in the model was recorded by a high-speed camera equipped with fluorescence microscope. As shown in Fig. S12, two kinds of oil droplets were formed in the model, one with diameter of ~10 μm (as pointed by green arrow) and the other with diameter of ~30 μm (as pointed by white arrow). The small droplets can shuttle between the pore freely and almost never get trapped by the throat (as displayed in Movie S2), whereas the pore-

scale droplets have a poor mobility and are difficult to migrate downstream. It is worth noting that since the sporadic pore-scale droplets were not enough to produce a plugging effect, the sweep efficiency could not be improved, thus the production of pure alkanes scarcely increased compare to blank control. This situation is also reflected in the ΔP. As can be seen in Fig. S13a, when NAS solution was injected, the ΔP was stable at ~2 kPa, even smaller than that in control case (~4 kPa), suggesting that the plugging effect did not exist in this system.

Supplementary video related to this article can be found at https://doi.org/10.1016/j.petsci.2021.11.014

Similarly, for NAS/aromatics system, emulsion was collected in the eluate (Fig. S11d), but significantly less than that of the NAS/alkanes group. As depicted in Table 2, only 25 μL emulsion was produced, which can also be explained by the greater viscosity of aromatics.

The resulting steady-state phase distribution in the porous medium is presented in Fig. 10. 3D high resolution images enable quantitative analysis of the intricate morphologies of the trapped oil ganglia at each flow condition. It is observed that the volume of trapped ganglia falls as capillary number rises (the N_c of each group is summarized in Table S2). The oil saturation was calculated by image analysis using ImageJ software. As can be seen in Fig. 10 and Table S2, the alkanes saturation decreased from 79% to 33% as the N_c rise from 1.4×10^{-6} to 3.3×10^{-5}. Similarly, for NAS/aromatics system, the oil saturation decreased from 81% to 47% as the N_c rise from 1.3×10^{-6} to 3.4×10^{-5}. As surfactant solution was injected, only small ganglia remain trapped. The capillary number is large enough to mobilize large ganglia. For example, when pure water was injected, the trapped ganglia typically take up more than 10 pore space (Fig. 10a and b). In contrast, after NAS displacement, the volume of the residual ganglia was generally less than 4 pore-space (Fig. 10c and d). For the missing ganglia, according to Fig. S11, S12, and Movie S2, we have adequate reasons to believe that they have been emulsified and displaced. To sum up, injection tests in the 3D model show that in-situ emulsification can significantly reduce residual oil saturation through entrainment effect, leading to improved oil recovery.

4. Conclusions

This work focused on the interaction between NAS solution and petroleum components at micron- and nano-scale, so as to reveal the mechanism of surfactant EOR without ultra-low IFT. At the nano-scale, micellar solubilization was proved to play an important role during the surfactant EOR process. The solubilization capacity of NAS micelles for petroleum fraction was determined by light absorbtion strategy, from which we can speculate that 1 ton of
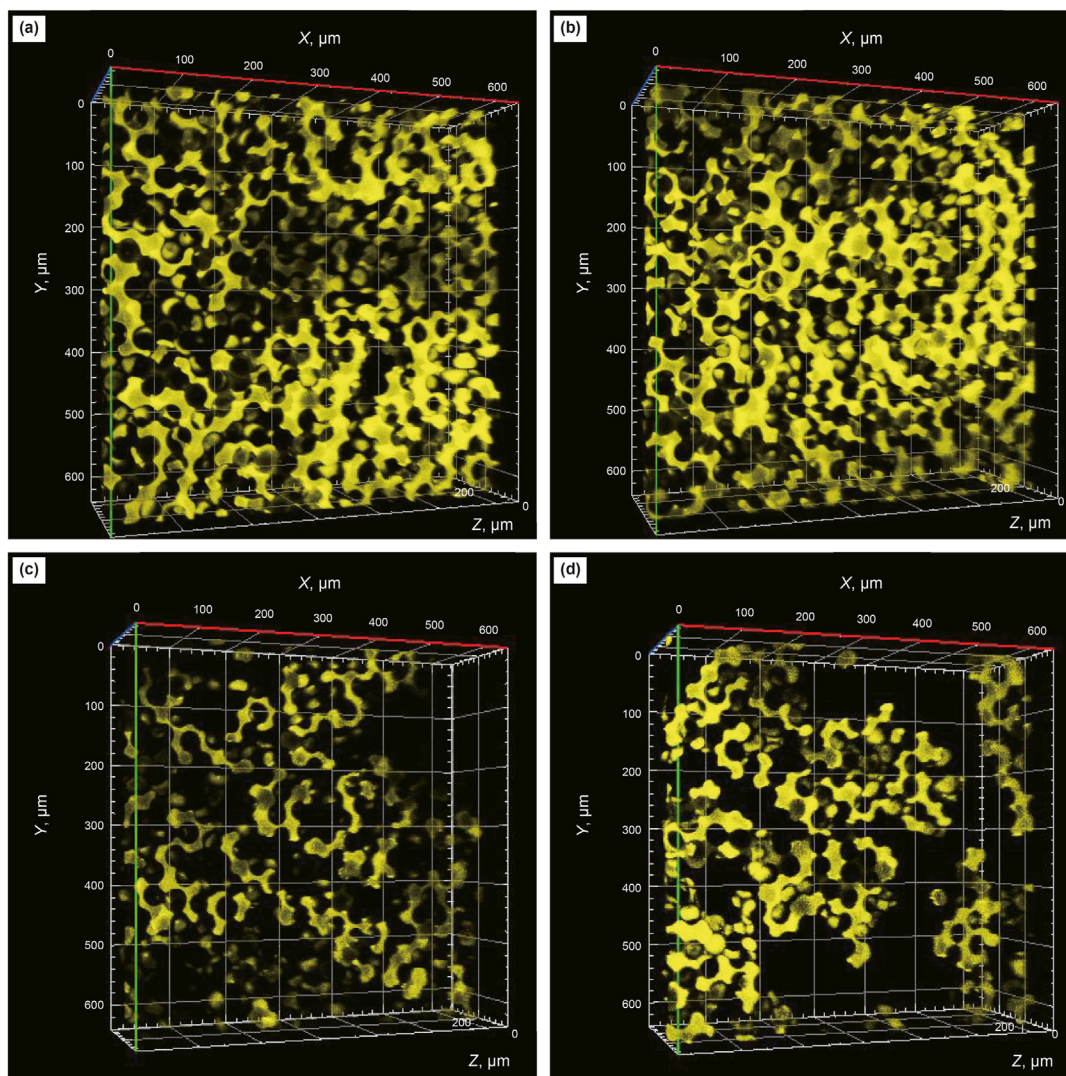
Fig. 10. 3D rendering of the residual (**a** & **c**) alkanes and (**b** & **d**) aromatics after (**a** & **b**) water and (**c** & **d**) 0.2 wt% NAS flooding. $\lambda_{ex} = 488$ nm. Displacing fluid was injected continuously at 10 μl·min^{-1} at 40 °C.

Table 2
Types of displacing and displaced phase and the displacement results in 3D micromodel.

Run	C_{NAS}, wt.%	Oil	Emulsion volume, μL	Oil volume, μL	Total volume, μL	Oil Saturation, %
1	0	alkanes	0	233	233	79%
2	0.2	alkanes	119	238	357	33%
3	0	aromatics	0	226	226	81%
4	0.2	aromatics	25	232	257	47%

0.2 wt% NAS displacing fluid can solubilize 780 g alkanes or 670 g aromatics in the field application. UV−Vis tests exhibit that aromatics is solubilized in the micellar core, while alkanes reside in the palisade layer. At the micron-scale, in-situ emulsification was investigated by using both 2D and 3D microfluidic devices. The tests in heterogeneous 2D chip show that the main mechanism of O/W emulsification was the snapping action at pore throat. The emulsion could plug the dominant route so as to divert the subsequent driving fluid to sweep more permeable region, which optimized the sweep efficiency, leading to an incremental alkanes of 26% and aromatics of 23% compared to waterflooding. Moreover, NAS solution could penetrate into the trapped oil to form W/O emulsion, which squeezes the oil-occupied space, and finally pushing 12% of trapped alkanes and 10% of aromatics to flow to main paths and be displaced. Further tests were conducted in a 3D model, and the results show that emulsification-entrainment effect can significantly reduce the residual oil saturation by 46% for NAS/ alkanes system and 34% for aromatics group.

These findings help understanding of the interaction between surfactant solution and crude oil before the formation of micro-emulsion, revealing the role of micellar solubilization and in-situ emulsification on oil displacement at low surfactant concentration and presenting a new strategy for designing surfactant-based displacing system for EOR process. However, despite both the 2D

and 3D models can simulate the underground porous media to a certain extent, the permeability of these chips is much higher than that of the realistic reservoir due to the limitation of etching techniques and the size of glass beads. Therefore, further work should focus on the preparation of micromodels with permeability comparable to the actual reservoir.

Author contributions

The manuscript was written through contributions of all authors. All authors have given approval to the final version of the manuscript.

Acknowledgements

Appendix A. Supplementary data

Supplementary data to this article can be found online at https://doi.org/10.1016/j.petsci.2021.11.014.

References

Aoudia, M., Al-Shibli, M.N., Al-Kasimi, L.H., Al-Maamari, R., Al-Bemani, A., 2006. Novel surfactants for ultralow interfacial tension in a wide range of surfactant concentration and temperature. J. Surfactants Deterg. 9, 287–293. https://doi.org/10.1007/s11743-006-5009-9.

Bera, A., Mandal, A., 2015. Microemulsions: a novel approach to enhanced oil recovery: a review. J. Petrol. Explor. Pord. Technol. 5, 255–268. https://doi.org/10.1007/s13202-014-0139-5.

Berg, S., Ott, H., Klapp, S.A., Schwing, A., Neiteler, R., Brussee, N., Makurat, A., Leu, L., Enzmann, F., Schwarz, J.O., Kersten, M., Irvine, S., Stampanoni, M., 2013. Real-time 3D imaging of Haines jumps in porous media flow. Proc. Natl. Acad. Sci. Unit. States Am. 110, 3755–3759. https://doi.org/10.1073/pnas.1221373110.

Broens, M., Unsal, E., 2018. Emulsification kinetics during quasi-miscible flow in dead-end pores. Adv. Water Resour. 113, 13–22. https://doi.org/10.1016/j.advwatres.2018.01.001.

Chatzis, I., Morrow, N.R., 1984. Correlation of capillary number relationships for sandstone. SPE J. 24, 555–562. https://doi.org/10.2118/10114-PA.

Chen, T., Chakrabarty, T., Cullen, M.P., Thomas, R.R., Sieben, M.C., 1991. Laboratory and field evidence of emulsion flow in porous media. In: CIM/AOSTRA Technical Conference, 21–24 April. Banff. https://doi.org/10.2118/91-78.

Chen, Z., Dong, M., Husein, M., Bryant, S., 2018a. Effects of oil viscosity on the plugging performance of oil-in-water emulsion in porous media. Ind. Eng. Chem. Res. 57, 7301–7309. https://doi.org/10.1021/acs.iecr.8b00889.

Chen, Z., Han, X., Kurnia, I., Yu, J.J., Zhang, G.Y., Li, L., 2018b. Adoption of phase behavior tests and negative salinity gradient concept to optimize Daqing oilfield alkaline-surfactant-polymer flooding. Fuel 232, 71–80. https://doi.org/10.1016/j.fuel.2018.05.130.

Chiang, C.L., 2001. Controlled growth of gold nanoparticles in AOT/C12E4/Isooctane mixed reverse micelles. J. Colloid Interface Sci. 239, 334–341. https://doi.org/10.1006/jcis.2001.7590.

Datta, S.S., Chiang, H., Ramakrishnan, T.S., Weitz, D.A., 2013. Spatial fluctuations of fluid velocities in flow through a three-dimensional porous medium. Phys. Rev. Lett. 111, 064501. https://doi.org/10.1103/PhysRevLett.111.064501.

Datta, S.S., Dupin, J.B., Weitz, D.A., 2014. Fluid breakup during simultaneous two-phase flow through a three-dimensional porous medium. Phys. Fluids 26, 022002. https://doi.org/10.1063/1.4884955.

de Haas, T.W., Fadaei, H., Guerrero, H., Sinton, D., 2013. Steam-on-a-chip for oil recovery: the role of alkaline additives in steam assisted gravity drainage. Lab Chip 13, 3832–3839. https://doi.org/10.1039/C3LC50612F.

do Nascimento, D.F., Vimieiro, J.R., Paciornik, S., Carvalho, M.S., 2019. Pore scale visualization of drainage in 3D porous media by confocal microscopy. Sci. Rep. 19, 12333. https://doi.org/10.1038/s41598-019-48803-z.

Foster, W.R., 1973. A low-tension waterflooding process. J. Petrol. Technol. 25, 205–210. https://doi.org/10.2118/3803-PA.

Gbadamosi, A.O., Junin, R., Manan, M.A., Agi, A., Yusuff, A.S., 2019. An overview of chemical enhanced oil recovery: recent advances and prospects. Int. Nano Lett. 9, 171–202. https://doi.org/10.1007/s40089-019-0272-8.

Gogarty, W.B., Meabon, H.P., 1970. Mobility control design for miscible-type waterfloods using micellar solution. J. Petrol. Technol. 22, 141–147. https://doi.org/10.2118/1847-E-PA.

Gong, L.Y., Liao, G.Z., Chen, Q.S., Luan, H.X., Feng, Y.J., 2019. Swollen surfactant micelles: properties and applications. Acta Phys. Chim. Sin. 35, 816–828. https://doi.org/10.3866/PKU.WHXB201810060 (in Chinese).

Gong, L.Y., Liao, G.Z., Luan, H.X., Chen, Q.S., Nie, X.B., Liu, D., Feng, Y.J., 2020. Oil solubilization in sodium dodecylbenzenesulfonate micelles: new insights into surfactant enhanced oil recovery. J. Colloid Interface Sci. 569, 219–228. https://doi.org/10.1016/j.jcis.2020.02.083.

Guillen, V.R., Carvalho, M.S., Alvarado, V., 2012a. Pore scale and macroscopic displacement mechanisms in emulsion flooding. Transport Porous Media 94, 197–206. https://doi.org/10.1007/s11242-012-9997-9.

Guillen, V.R., Remero, M.I., Carvalho, M.S., Alvarado, V., 2012b. Capillary-driven mobility control in macro emulsion flow in porous media. Int. J. Multiphas. Flow 43, 62–65. https://doi.org/10.1016/j.ijmultiphaseflow.2012.03.001.

Guo, H., Li, Y.Q., Wang, F.Y., Yu, Z.Y., Chen, Z.W., Wang, Y.S., Gao, X., 2017. ASP flooding: theory and practice progress in China. J. Chem. 2107, 8509563. https://doi.org/10.1155/2017/8509563.

Hayter, J.B., Penfold, J., 1981. An analytic structure factor for macroion solutions. Mol. Phys. 42, 109–118. https://doi.org/10.1080/00268978100100091.

Healy, R.N., Ree, R.L., 1977. Immiscible microemulsion flooding. SPE J. 17, 129–139. https://doi.org/10.2118/5817-PA.

Hirasaki, G.J., Miller, C.A., Raney, O.G., Poindexter, M.K., Nguyen, D.T., Hera, J., 2011. Separation of produced emulsions from surfactant enhanced oil recovery processes. Energy Fuels 25, 555–561. https://doi.org/10.1021/ef101087u.

Hu, G., Ma, D., Wang, H., Wang, F., Gu, Y., Yu, Z., Wang, Y., Li, Y., 2017. Proper use of capillary number in chemical flooding. J. Chem. 2017, 4307368. https://doi.org/10.1155/2017/4307368.

Jeirani, Z., Jan, B.M., Ali, B.S., See, C.H., Saphanuchart, W., 2014. Pre-prepared microemulsion flooding in enhanced oil recovery: a review. Petrol. Sci. Technol. 32, 180–193. https://doi.org/10.1080/10916466.2011.586968.

Jeirani, Z., Jan, B.M., Ali, B.S., Noor, I.M., See, C.H., Saphanuchart, W., 2013. Formulation, optimization and application of triglyceride microemulsion in enhanced oil recovery. Ind. Crop. Prod. 43, 6–14. https://doi.org/10.1016/j.indcrop.2012.07.002.

Klier, J., Tucker, C.J., Kalantar, T.H., Green, D.P., 2000. Properties and applications of microemulsions. Adv. Mater. 12, 1751–1757. https://doi.org/10.1002/1521-4095(200012)12:23<1751::AID-ADMA1751>3.0.CO;2-I.

Kokal, S.L., Maini, B.B., Woo, R., 1992. Flow of emulsions in porous media. In: Schramm, L.L. (Ed.), Emuldions. American Chemical Society, Washington DC, pp. 219–262. https://doi.org/10.1021/ba-1992-0231.ch006.

Lindén, M., Agren, P., Karlsson, S., 2000. Solubilization of oil in silicate-surfactant mesostructures. Langmuir 16, 5831–5836. https://doi.org/10.1021/la991671h.

Liu, J., Sheng, J.J., Tu, J., 2020. Effect of spontaneous emulsification on oil recovery in tight oil-wet reservoirs. Fuel 279, 118456. https://doi.org/10.1016/j.fuel.2020.118456.

Liu, Z.Y., Li, Y.Q., Luan, H.X., Gao, W.B., Guo, Y., Chen, Y.H., 2019. Pore scale and macroscopic visual displacement of oil-in-water emulsions for enhanced oil recovery. Chem. Eng. Sci. 197, 404–414. https://doi.org/10.1016/j.ces.2019.01.001.

Luan, H.X., Gong, L.Y., Yue, X.J., Nie, X.B., Chen, Q.S., Guan, D., Que, T.L., Liao, G.Z., Su, X., Feng, Y.J., 2019. Micellar aggregation behavior of alkylaryl sulfonate surfactants for enhanced oil recovery. Molecules 24, 4325–4338. https://doi.org/10.3390/molecules24234325.

McAuliffe, C.D., 1973. Oil-in-water emulsion and their flow properties in porous media. J. Petrol. Technol. 25, 727–733. https://doi.org/10.2118/4369-PA.

Nguyen-Kim, V., Prévost, S., Seidel, K., Maier, W., Marguerre, A.K., Oetter, G., Tadros, T., Gradzielski, M., 2016. Solubilization of active ingredients of different polarity in Pluronic® micellar solutions—correlations between solubilizate polarity and solubilization site. J. Colloid Interface Sci. 477, 94–102. https://doi.org/10.1016/j.jcis.2016.05.017.

Rosen, M.J., Kunjappu, J.T., 2012. Surfactants and Interfacial Phenomena, fourth ed. John Wiley & Sons, New Jersey.

Sheng, J.J., 2015. Status of surfactant EOR technology. Petroleum 1, 97–105. https://doi.org/10.1016/j.petlm.2015.07.003.

Sun, C., Guo, H., Li, Y.Q., Song, K.Q., 2020. Recent advances of surfactant-polymer (SP) flooding enhanced oil recovery field tests in China. Geofluids 2020, 8286706. https://doi.org/10.1155/2020/8286706.

Tehrani-Bagha, A.R., Holmberg, K., 2013. Solubilization of hydrophobic dyes in surfactant solutions. Materials 6, 580–608. https://doi.org/10.3390/ma6020580.

Tehrani-Bagha, A.R., Singh, R.G., Holmberg, K., 2012. Solubilization of two organic dyes by cationic ester-containing gemini surfactants. J. Colloid Interface Sci. 376, 112–118. https://doi.org/10.1016/j.jcis.2012.02.016.

Thomas, S., 2008. Enhanced oil recovery-an overview. Oil Gas Sci. Technol. 63, 9–19. https://doi.org/10.2516/ogst:2007060.

Torchilin, V.P., 2007. Micellar nanocarriers: pharmaceutical perspectives. Pharm Res-Dordr. 24, 1. https://doi.org/10.1007/s11095-006-9132-0.

Vermathen, M., Louie, E.A., Chodosh, A.B., Ried, S., Simonis, U., 2000. Interactions of water-insoluble tetraphenylporphyrins with micelles probed by UV−Visible and NMR spectroscopy. Langmuir 16, 210–221. https://doi.org/10.1021/la990903+.

Wang, H., Cao, X., Zhang, J., Zhang, A., 2009. Development and application of dilute surfactant−polymer flooding system for Shengli oilfield. J. Petrol. Sci. Eng. 65, 45–50. https://doi.org/10.1016/j.petrol.2008.12.021.

Wu, H., Kawaguchi, S., Ito, K., 2005. ^{1}H NMR studies on intermolecular association of amphiphilic cationic polyelectrolyte micelles induced by hydrophobic counter

anions in water. Colloid Polym. Sci. 283, 636–645. https://doi.org/10.1007/s00396-004-1194-0.

Zhao, R., Huang, H., Wang, H., Zhang, J., Zhang, L., Zhang, L., Zhao, S., 2013. Effect of organic additives and crude oil fractions on interfacial tensions of alkylbenzene sulfonates. J. Dispersion Sci. Technol. 34, 623–631. https://doi.org/10.1080/01932691.2012.685844.

Zhao, X.Z., Deng, K.C., Liu, F.J., Zhang, X.L., Yang, H.R., Peng, J.L., Liu, Z.K., Ma, L.W., Wang, B.Y., Wei, H., 2018. Fabrication of conjugated amphiphilic triblock copolymer for drug delivery and fluorescence cell imaging. ACS Biomater. Sci. Eng. 4, 566–575. https://doi.org/10.1021/acsbiomaterials.7b00991.

Zhao, X.Z., Feng, Y.J., Liao, G.Z., Liu, W.D., 2020. Visualizing in-situ emulsification in porous media during surfactant flooding: a microfluidic study. J. Colloid Interface Sci. 578, 629–640. https://doi.org/10.1016/j.jcis.2020.06.019.

Zhao, X.Z., Gong, L.Y., Liao, G.Z., Luan, H.X., Chen, Q.S., Liu, D., Feng, Y.J., 2021. Micellar solubilization of petroleum fractions by heavy alkylbenzene sulfonate surfactant. J. Mol. Liq. 329, 115519. https://doi.org/10.1016/j.molliq.2021.115519.

Zhu, Y., Jian, G., Liu, W., Cheng, L., Hou, Q., Li, J., 2013. Recent progress and effects analysis of surfactant-polymer flooding field tests in China. In: SPE Enhanced Oil Recovery Conference. Kuala Lumpur. https://doi.org/10.2118/165213-MS, 2–4 July.